Utrecht University

Faculty of Science
Debye Institute

Measuring point spread functions and calibrating (STED) confocal microscopes

Bachelor thesis

Peter N.A. Speets

Physics and Astronomy

main supervisors

Prof.dr. Alfons van Blaaderen
Soft Condensed Matter Group

Dr. Arnout Imhof
Soft Condensed Matter Group

daily supervisor

Ernest B. van der Wee
Soft Condensed Matter Group

June 2016

Abstract

In this thesis the point spread function (PSF) used to characterize a confocal microscope was determined for different configurations. The PSF was determined for a sample with a refractive index matched to the refractive index that the objective was designed for, which is in this case $n = 1.518$ and $n = 1.451$ [1], and it was investigated how a mismatch in refractive index affects the shape and size of the PSF. Also the PSF of stimulated emission depletion (STED) confocal microscopy was determined to investigate the advantages of STED over conventional confocal microscopy. The alignment of the STED and the excitation laser of the confocal microscope was checked by imaging the reflection of the STED and excitation laser with a gold core nanoparticle. For the calibration of the distance measurement in a sample with a mismatch in refractive index a colloidal crystal was grown to compare the interlayer distance determined by using FTIR spectroscopy and the interlayer distance determined by imaging the crystal with the confocal microscope.

1 Introduction

The purpose of confocal microscopy, compared to brightfield microscopy, is to increase resolution and contrast. The confocal microscope ensures that only light from the focus point in the sample is imaged. It eliminates the light originating from other spots in the sample by only illuminating the focus point, whereas conventional brightfield microscopes illuminate the whole sample, as is sketched in Figure 1a. The confocal microscope achieves this by having the light source in the focus point of the objective and blocking the light from other places in the sample by a pinhole, as can be seen in Figure 1b. Because the light source, the imaged spot and the detector are in focus, this is called confocal microscopy [2]. To make detection of light from such a small point possible, samples are dyed with fluorophores and the emitted light is detected.

Like all optical instruments, microscopes cannot have an indefinitely high resolution. Images made close to the maximum resolution of the microscope look blurred. The function by which an object is blurred is called the point spread function (PSF). The maximum resolution in the lateral direction, the direction parallel to the sample, as can be seen in Figure 1c, can be given by the Rayleigh diffraction limit. The Rayleigh criterion states that two point sources are discernible, if they are separated by at least one Airy disk [2]: $r_{Rayleigh} = 0.61\lambda/n \sin\alpha$. With λ the wavelength of the detected light and n the refractive index of the sample and α the half angle of a convergent light cone [2], as can be seen in Figure 1b. $n \sin\alpha$ is called the numerical aperture (NA) and is a property of the used objective lens to describe the convergence of the light cone. The radius is taken to be the distance between the center and its first maximum of the Airy disk. For light with a wavelength of $\lambda = 495$ nm and an objective with a numerical aperture of 1.4 the resolution in the lateral direction is 216 nm. In the 19^{th} century this was regarded as the maximum achievable resolution dictated by physics [3]. For the axial direction the microscope has a resolution of 750 nm. The resolution of a confocal microscope can be a factor $\sqrt{2}$ higher than a conventional microscope, if an infinitely small pinhole diameter is assumed [4]. This results in a resolution of a confocal microscope of 150 nm in the lateral direction and 532 nm in the axial direction [4].

To further increase the resolution beyond Rayleigh's diffraction limit super-resolution techniques, such as stimulated emission depletion (STED) [5], can be used. For the development of STED microscopy S.W. Hell received a shared Nobel Prize [6]. STED microscopy uses a second laser next to the excitation laser. A STED confocal setup is sketched in Figure 2. This doughnut shaped STED beam depletes the fluorophores around the focus point by triggering a stimulated emission of a photon of the same wavelength and direction as the STED beam. This is sketched in Figure 3. Because the depleted fluorophores in the volume around the focus point do not emit light in the wavelength of the spontaneous excitation, but the fluorophores at the focus point still do, the resolution is further increased. The resolution of a STED microscope can be changed so that either the axial resolution is improved or the lateral resolution. The maximum lateral resolution is about 20 to 100 nm [5] [4] and the maximum axial resolution is about 100 nm[7] [4].

For any microscope that is not designed for a mismatch of refractive index, it is imperative for the resolution in the z-direction to match the refractive index of the sample to the refractive index of the objective. This is important, because a mismatch in refractive index increases the blurring of the image, because the rays in center of the light cone are focussed on a different point than the rays at the periphery of the light cone. The mismatch also changes the focus point in the z-direction, because of the same effect that make partly immersed objects look bend.

In this research the PSF is determined for both a matched refractive index within the whole sample and a mismatch in refractive index between the sample and the refractive index that the objective is designed for. This is done with a glycerol/water sample with a refractive index of $n_D^{20} = 1.451$ and an oil sample with a refractive index of $n_D = 1.516$ [4] imaged with a glycerol objective and an oil objective. For a matched sample the effect of the pinhole on the size of the PSF is investigated. Also the effect of STED microscopy on the size of the PSF is investigated, as well as the alignment of the STED and the excitation laser. To check the calibration of the distance of the confocal microscope, a close packed colloidal crystal was grown. Because of the regular interlayer distance, this can be used as a method to calibrate the microscope for different refractive indices.

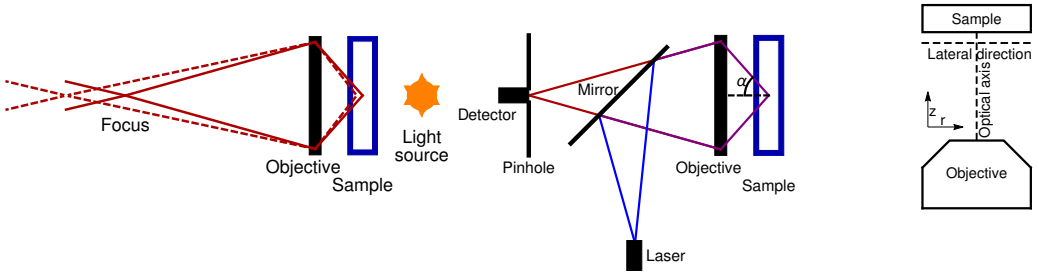

(a) Conventional microscope **(b)** Confocal microscope **(c)** Optical and lateral axes

Figure 1 – Sketch of a conventional microscope and a confocal microscope and the used axes and coordinates.

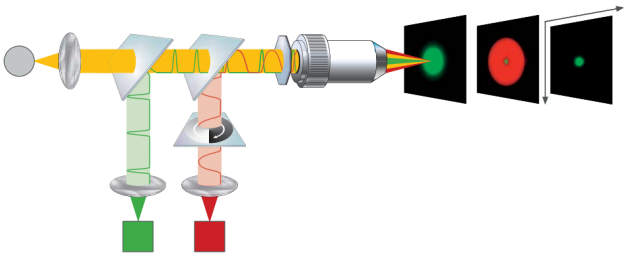

Figure 2 – Sketch of a STED microscopy setup. The depletion beam (red) is superimposed onto the excitation beam (green), therefore decreasing the volume in which spontaneous emission can take place. Figure a by Leica, Germany [8]

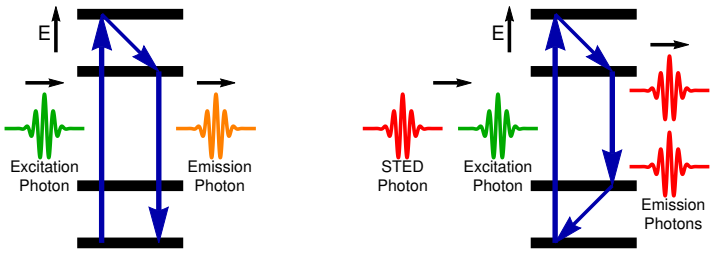

(a) Spontaneous emission **(b)** Stimulated emission

Figure 3 – Energy diagrams of spontaneous and stimulated emission. Figure a is a sketch of the energy diagram of spontaneous emission and Figure b of stimulated emission.

2 Theory

2.1 Convolution and deconvolution

A microscope image is a convolution of the point spread function of the microscope with the imaged object plus additional noise[2]. This object can be for example a colloidal particle. This means the image is actually a blurred picture of the object. If a known object is imaged, any difference between the object and the obtained image is caused by the PSF and (detector)noise [2].

$$object \circledast \text{PSF} + noise = image \tag{2.1}$$

The image can be deconvolved by taking the Fourier transform, because in Fourier space the convolution product can be evaluated as an ordinary product [9]. The PSF can be obtained by taking the Fourier transform of the image and the object, in this case a spherical particle. The noise term affects the level of detail that the deconvolved image will have.

$$\begin{aligned} \mathcal{F}(\text{PSF}) &= \mathcal{F}(image - noise)/\mathcal{F}(object) \\ \mathcal{F}(object) &= \mathcal{F}(image - noise)/\mathcal{F}(\text{PSF}) \end{aligned} \tag{2.2}$$

2.2 The point spread function (PSF)

The point spread function of a brightfield microscope in the lateral plane can be estimated by an Airy function with $k = 2\pi r\text{NA}/\lambda$ and $J_1(k)$ a Bessel function of the first kind [4]. In this equation k is the dimensionless distance scale, NA the numerical aperture and λ the wavelength of the emitted light [4].

$$I_{xy} = I_0 \left(\frac{2J_1(k)}{k} \right)^2 \tag{2.3}$$

In axial direction the PSF can approximated by:

$$I_z = \left(\frac{\sin(u/4)}{u/4} \right)^2 \tag{2.4}$$

With $u = 2\pi\text{NA}^2 z/(\lambda n)$. The advantage of this approximation is that in the lateral plane this approximation exhibits the same features as an experimental PSF. Because a confocal microscope only illuminates the focus point, the PSF of a confocal microscope is approximately the square of the brightfield PSF[2]:

$$\text{PSF}_{confocal} \approx \text{PSF}^2_{brightfield} \tag{2.5}$$

This should increase the resolution with maximum a factor $\sqrt{2}$. The factor $\sqrt{2}$ cannot be achieved, however, because this assumes an infinitely small pinhole. Of course, also the wavelength of the excitation beam is different than the wavelength of the emitted light. The advantage over conventional microscopy is its increase in resolution and contrast, because the out of focus light is removed. To take the pinhole into account the PSF is convolved with the area of the pinhole. Unfortunately, the Airy disk approximation assumes a low numerical aperture, which is not valid in most situations as the resolution increases with a higher numerical aperture. A better approximation which does not assume low numerical aperture is the PSF described in Appendix Appendix B. The resulting formulas, however, cannot be calculated exactly because the integral is over Bessel functions, but this approximation is used to numerically calculate the simulated PSF of Figure 4a and 4b. The images in Figure 4c and 4d are a convolution of this PSF and a spherical particle of 200 nm. This calculation is done with a numerical aperture of 1.4. For simplicity the wavelength of $\lambda = 495$ nm is chosen for both the excitation laser and the fluorescence of the dye in this simulation. Figure 4e and 4f is a simulated image that also includes Poisson noise with a signal to noise ratio of 5.4 added with the *ImageEffect* function of Wolfram Mathematica.

2.3 The signal to noise ratio

Because the detection of photons is distributed as a Poisson distribution [2], the signal to noise ratio (SNR) is for the high noise case the square root of the total amount of incoming photons. The noise caused by the quantification of light by photons is thus $\sqrt{n_{photons}}$ [2]. This is not the same as background noise or detector noise, which is not dependent on the amount of detected photons. An example of how the Poisson noise affects the image is shown in Figure 4. The image of Figure 4e and 4f is the same convolution of Figure 4c and 4d but with added noise.

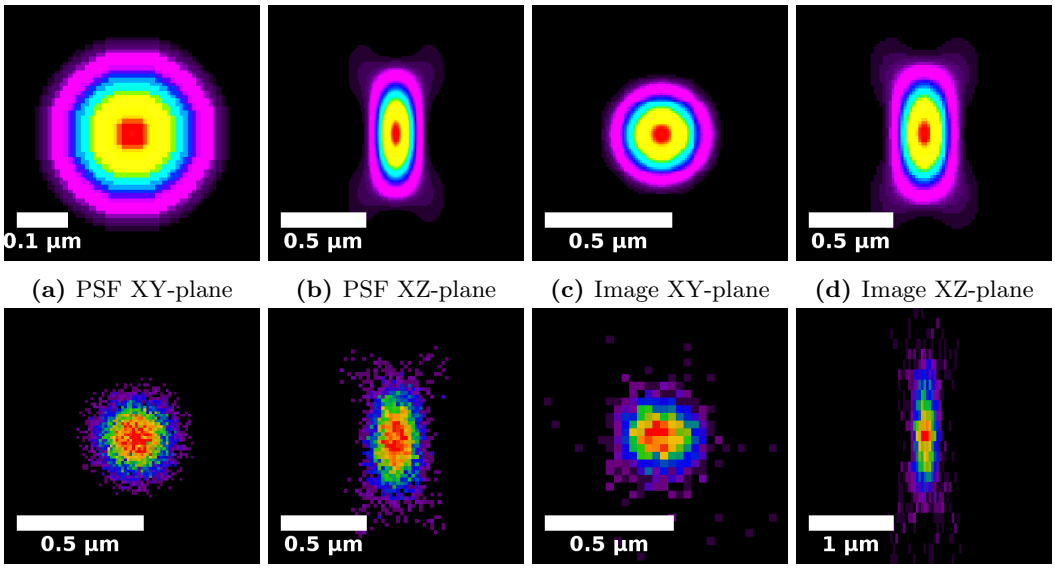

(a) PSF XY-plane **(b)** PSF XZ-plane **(c)** Image XY-plane **(d)** Image XZ-plane

(e) Image XY-plane **(f)** Image XZ-plane **(g)** Confocal Image XZ-plane **(h)** Confocal Image XZ-plane

Figure 4 – Figure a and b show a confocal PSF calculated with with the approximation given in Appendix Appendix B [2] using a wavelength of $\lambda = 495$ nm and a numerical aperture of 1.4 and a refractive index of 1.518. Figure c and d are images calculated form a convolution of the PSF of Figure a and b and a spherical object of 200 nm in diameter. Figure e and f is the same convolution as Figure c and d with added Poisson noise with a SNR of 5.4. For comparison the images in Figure g and h are confocal images imaged under the same conditions, but with a different sampling rate. The pixel size is 30 nm. The size of the simulated PSF is 140 nm in the lateral direction and 350 nm in the axial direction. This is much smaller than the experimental PSF.

2.4 Effect of mismatch in refractive index

A mismatch in refractive index between the refractive index that the objective is designed for, and the sample has negative effects on the size and shape of the PSF. In Figure 5 the beam paths of a mismatched sample is sketched. The mismatch causes a change in effective numerical aperture. This makes the PSF to become larger because of the dependence on NA of Equation 2.3 and 2.4. Furthermore the mismatch in refractive index causes the focus of the outer rays to be different than the inner rays, causing a distortion similar to spherical aberration of the lens. The axial distances in the sample are also elongated or shrunk as in Figure 5. Through geometrical optics a scaling factor can be derived [4] [10]:

$$\Delta z_{focus} = \Delta z_{objective} \sqrt{\frac{n_1^2 - \mathrm{NA}^2}{n_2^2 - \mathrm{NA}^2}} \tag{2.6}$$

Here is Δz_{focus} the distance from the interface between the media with refractive indices of n_1 and n_2 and $\Delta z_{objective}$ the distance of the objective lens to bring Δz_{focus} in focus. According Besseling [4] this on geometrical optics based formula does not hold. The experimental scaling factor found by Besseling is:

$$\Delta z_{focus} = \Delta z_{objective}(0.82 n_2 - 0.24) \tag{2.7}$$

For an objective with numerical aperture 1.4 and a refractive index of the immersion oil of $n_D = 1.516$.

The effect of the mismatch in refractive index on the PSF can be calculated with the formula's described in Appendix Appendix C [11]. For this derivation Sheppard *et al.* take the vectorial properties of the light into account, as opposed to the purely geometrical sketch of Figure 5.

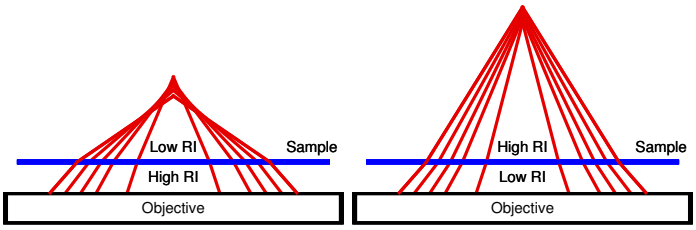

Figure 5 – Sketch of spherical aberration and the effect of a mismatch in refractive index on the axial position of the focus point and the effective numerical aperture.

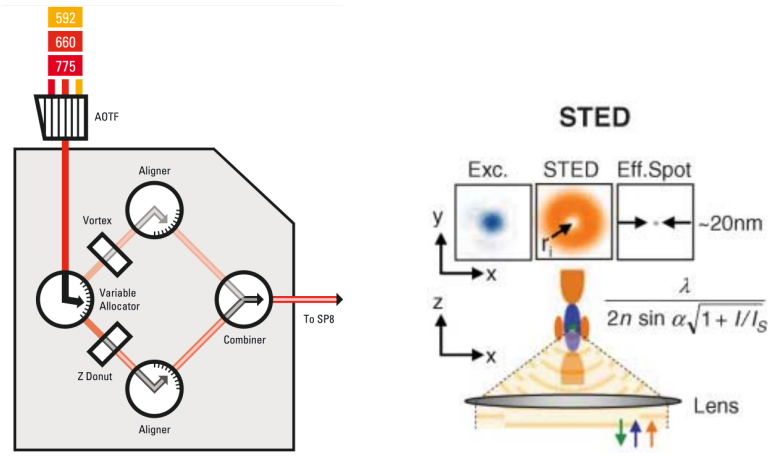

(a) **(b)**

Figure 6 – In Figure a is sketched how the shape of the STED beam changes by altering the z parameter. This changes the fraction of the light that is passing through the vortex plate and the z doughnut phase mask. Image by Leica, Germany [14]. In Figure b the shape of the excitation and the depletion laser of a STED confocal setup for 2D STED (above) and 3D STED (below) is sketched. The doughnut shaped depletion laser is superimposed onto the excitation beam, so the fluorophores in the periphery of the focus spot do not emit fluorescent light. Image by S.W. Hell [15].

2.5 Stimulated emission depletion (STED)

The resolution of the confocal microscope can be increased with the use of STED with a setup sketched in Figure 2. The doughnut shaped STED beam depletes the fluorophores around the focus point, but not in the focus point itself. In Figure 3a and 3b the energy diagram of spontaneous and stimulated emission are sketched. The STED beam kicks the excited electron back to a lower energy level creating a second photon with the same wavelength as the STED photon and propagating in the same direction. In the lateral plane the resolution of STED microscopy is [12] [13]:

$$r_{\text{STED}} = \frac{\lambda}{2n \sin\alpha \sqrt{1 + \frac{I}{I_s}}} \tag{2.8}$$

In this equation is I the STED laser intensity and I_s is the saturation intensity of the fluorophore. The STED beam passes a phase mask to cause destructive interference at the focus point [14], as is sketched in Figure 6. The beam can be split between two phase masks so the shape of the STED laser beam can be altered to increase either the axial or the lateral resolution. If this z parameter is 0 the lateral resolution is maximized and when this value is 1 the axial resolution is maximized. A z parameter of 0.6 is often used as compromise. The shape of the excitation and depletion lasers in focus is shown in Figure 6b.

2.6 A colloidal crystal

A hard sphere colloidal crystal forms a closely packed hexagonal lattice with either face centred cubic (FCC) or hexagonal close packed (HCP) ordering [16]. For a colloidal crystal the band

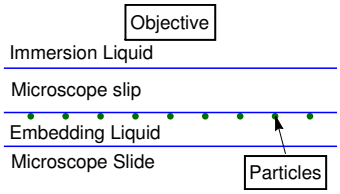

Figure 7 – Sketch of a typical sample.

gap due to Bragg scattering is within the infra red spectrum [16]. The wavelength of the gap in the transmission spectrum is $\lambda = n_{eff}\sqrt{2/3}D$ [16] with D the diameter of the particles. In this formula n is the refractive index of the particles and the medium within the crystal, in this case air, combined. This effective refractive index can be calculated using the weighted average of the square of the refractive index: $n_{eff} = \phi n^2_{particle} + (1-\phi)n^2_{medium}$ [17]. Here ϕ is the volume fraction. The interlayer spacing is $d_{111} = \sqrt{2/3}D$. The packing fraction of a closely packed lattice is 74% [18]. This yields an effective refractive index of n = 1.33. This is close to the upper limit of the effective refractive index of a colloidal crystal of silica particles and air of n = 1.335 found by Thijssen [18].

The number of particle layers that are deposited in a process of controlled drying is according to Jiang *et al.* [16]:

$$N_{layers} = \frac{\beta L \phi}{0.605\, D(1-\phi)} \tag{2.9}$$

With L the height in which the evaporation takes place. This is 310 μm [16] for ethanol. D is the particle diameter, ϕ the volume fraction and β the ratio between the speed of the particles within the solvent and the solvent itself. Because the suspension is stationary β is assumed to be 1.

3 Methods

3.1 Sample for PSF measurement

A typical sample is sketched in Figure 7. The samples used to image the particles are made by pipetting a solution of the used particles onto a microscope slide and evaporating the solvent in a drying oven with a temperature of 50° C. For the samples used for imaging with a refractive index mismatch between the used objective and the sample the particles were dried onto the cover slip. Hereafter a droplet of the embedding medium was placed onto the microscope slide. The embedding medium was chosen such that it matches the refractive index of the cover slip. This embedding medium can either be Leica type F immersion oil with a refractive index of $n_D^{23} = 1.516$ [4] or a glycerol/water mixture with a volume fraction glycerol of 85% with a refractive index of $n_D^{20} = 1.451$ measured with an Abbe refractometer (Atago NAR 3T). Then the cover slip was placed onto a microscope slide. This cover slip can be either a Menzel Gläzer #1.5 cover slip with a thickness of approximately 170 μm with a refractive index close to the immersion oil or a fused silica cover slip with a refractive index of $n_D = 1.459$ [19]. The sample was sealed with Norland Optical adhesive UV glue, so the immersion liquid does not come into contact with air or leaks immersion liquid.

3.2 Particles

The particles used for this research are listed in Table 1. For the determination of the PSF for a confocal microscope YG Fluoresbrite particles from Polysciences [4] (Ps200) that consist of fluorescein isothiocyanate (FITC) dyed polystyrene with a diameter of 200 ± 10 nm [4] were used. It is doubted the immersion liquid does not affect the polystyrene particles. The immersion liquid could creep into the polystyrene and cause it to swell. Therefore the polystyrene samples were not used for longer than one day.

To measure the PSF of the STED setup and for the colloidal crystal silica particles were used. The silica particles were synthesised by growing a silica shell around a gold nanoparticle. The gold nanoparticle is synthesised according to the method described by Bastús *et al.* [20]. The silica shell was grown by adding gold nanoparticles to a solution of water and poly(vinyl-pyrrolidone) (PVP) [21]. The PVP adsorbs onto the gold particles. The gold particles are then

Particle	Material	Fluorophore	Diameter (nm)	Polydispersity
Ps200	Polystyrene	FITC	200	5.0% [4]
Si170	Silica	RITC	169	4.5%
Si250	Silica	RITC	237	4.1%
Si450	Silica	RITC	468	3.3%
Si600	Silica	RITC	607	5.3%

Table 1 – The particles used in this research. Particle diameter and polydispersity of the Si170 particles courtesy of Jantina Fokkema and the particle diameter of Si250, Si450 and Si600 particles courtesy of Marc Del Pozo Puig.

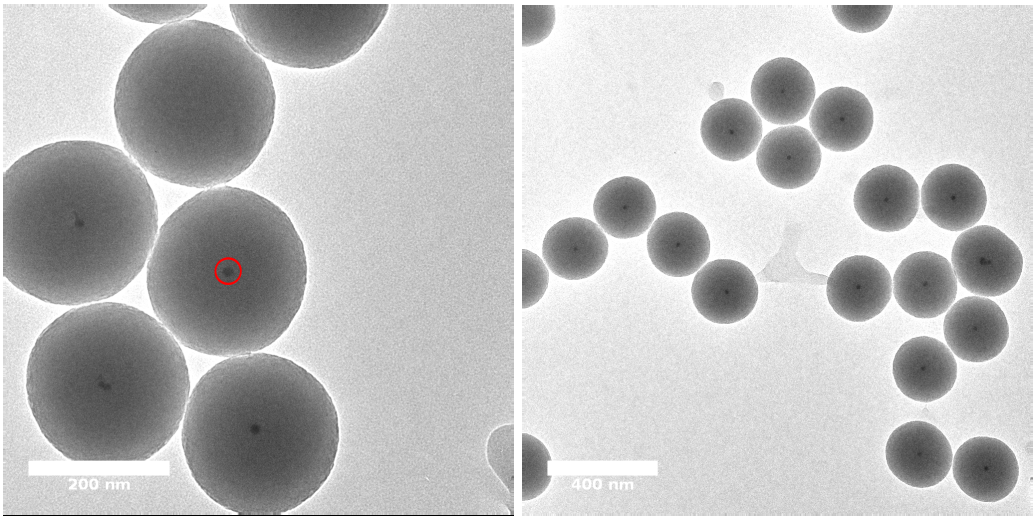

Figure 8 – TEM images of the particles used for the alignment test of the STED laser beam (Si250 particles). The particles consist of a gold core (encircled) and a silica shell. Images courtesy of Marc Del Pozo Puig.

transferred into an ethanol/ammonia solution with tetraethoxysilane (TEOS) $Si(O(C_2H_5)_4)$. The TEOS will deposit the silica onto the surface of the gold nanoparticle creating a silica shell around the particle [21]. The diameter and polydispersity of the resulting particles was determined by averaging the diameter of many particles obtained from transmission electron microscopy (TEM) images. In the particle is some solvent, because the particle is porous. Because for TEM it is needed to image the particle in vacuum, the solvent inside the particle evaporates. This causes the diameter of the particle to shrink when imaged from TEM, but this diameter provides a minimum bound for the particle diameter when imaged by a confocal microscope.

For the determination of the PSF of the STED setup silica particles with a diameter of 169.4 ± 7.7 nm were used (Si170). These particles have a gold core with a diameter of 43.9 ± 4.6 nm. The gold core absorbs light of wavelengths around the excitation wavelength of rhodamine isothiocyanate (RITC) [22]. The absorbed energy causes the fluorescent dye to emit more light. The gold cores also make imaging of the particle with reflected excitation laser light possible.

The alignment of the excitation and the STED beam was tested with RITC dyed silica particles with a gold core, Si250. Around the dyed silica shell a non dyed silica shell was grown as spacer, so there is always a minimum distance between two particles. This makes sure that particles that are next to each other are always recognized as two separate particles. For the colloidal crystal the this same method was used, but the undyed silica shell is much larger. For the colloidal crystal particles with a diameter of 607 ± 31nm and 468 ± 15nm, respectively Si600 and Si450 were used.

3.3 Microscope

In this project two microscopes were used. The Leica SP2 and the Leica SP8. The Leica SP2 is equipped with a photon multiplier tube (PMT). When a photon is detected by a PMT it first hits a photocathode [23]. This photocathode emits an electron when hit by a photon. This electron hits a negatively charged dynode, which emits more electrons when hit. Because these electrons also hit a dynode, one photon hit can cause an electron shower with a high enough intensity to

be detected. One photon hit is detected by approximately 10^6 electrons [23]. For de excitation of the FITC dyed polystyrene particles an ArKr laser with a wavelength of $\lambda = 488$ nm was used. The Leica SP8 is equipped with both PMT's and Hybrid Detectors (HyD). The HyD's are more sensitive and cause less detector noise, but are vulnerable to higher light intensities, so cannot be used to detect reflected laser light, but these detectors will be used for the detection of the emitted light. The HyD's use the same principle as PMT's, but they use an avalanche diode instead of dynodes to enhance the signal of a single electron from the photocathode [23]. The HyD also has gating, so that the HyD detector only measures light after the excitation laser excited a spot in the sample, decreasing the light that is not coming from the point of interest. The excitation laser of the SP8 is a white light laser (WLL) of NKT Photonics, so the wavelength is tunable. The laser beam was tuned to have a wavelength of $\lambda = 495$ nm to excite FITC dyed particles and $\lambda = 520$ nm for RITC dyed particles.

As immersion liquid for the oil objectives the Leica type F immersion oil was used. The immersion liquid for the glycerol objective is immersion oil with a refractive index of $n_D^{20} = 1.451$ produced by Cargille.

3.4 Imaging

The imaging of the particles was done with a sub-Nyquist resolution. This means that no extra information can be gained by increasing the resolution further. The Nyquist sampling rate was calculated by the Nyquist Calculator of SVI [24]. The Nyquist resolution for imaging with an oil objective with a numerical aperture of 1.4, an excitation wavelength of 495 nm and an emission wavelength of 520 nm the Nyquist sampling is 44 nm in the lateral direction and 132 nm [24].

The pinhole size was left on 1 AU (Airy unit) of an airy disk of $\lambda = 580$ nm light. The laser power varied, but a typical laser power lies around 5% of the maximum capacity. The gain of the detectors was set in such way that the histogram of the intensities used the full range peaks so no clipping occurred. A typical histogram is shown in Figure 9. Depending on how much signal the detectors received, imaging was done with a line average of $2\times$ to $4\times$. In case of a weak signal a frame was imaged $2\times$ to $4\times$ and the pixel values were accumulated effectively decreasing the scanning speed. The typical scanning speed was set to 400 Hz. For the Hybrid detector gating was enabled, so the detector detected only light from after excitation. The size of the imaged volume in the axial direction was 6 μm to include all information of the imaged particles. In case of a mismatch in refractive index the position of the interface between the cover slip and the embedding medium was determined by detecting reflected excitation laser light with PMT's.

To determine the PSF of the STED setup a Si170 sample was imaged with a $\lambda = 660$ nm continuous wave STED laser. The pinhole radius was automatically set by the software. The laser power was varied to investigate how the resolution changes due to the STED setup. To investigate the effect of the z parameter (not to be confused with the axial coordinate) that defines the shape of the STED beam near the focus point to increase either the axial or the lateral resolution, two extra PSF's are measured to check if there is an improvement or loss in the resolution when the z parameter was changed. The z parameter was set on 0 for the measurements with different laser powers and was set on 60% and 100% for two additional measurements to determine the resolution for a different z parameter.

For STED to be effective the both the excitation and the depletion beam should overlapping. To check the alignment of both beams, the reflectance of both beams on a gold core of 15.6 nm of a Si250 particle is imaged. The Leica SP8 has an option to automatically align the beams. To check the effect of the automatic alignment, the imaging was done both before and after the alignment.

3.5 Estimating the signal to noise ratio

To estimate the signal to noise ratio, two methods are used. The most straightforward method is to count the number of photons directly with the Hybrid Detectors on the SP8 microscope. This yields a maximum photon count for the Ps200 FITC dyed particles of 29 with a laser intensity of 10.5% of the maximum capacity. This means that the SNR is $\sqrt{29} = 5.4$. Unfortunately it was not not possible to directly count the number of photons with the PMT's. To give an estimate of the SNR with a PMT, it is possible to look how much signal corresponds to a single photon hit by considering the intensity peaks that occur in the dark regions of the image [25]. In Figure 10 a profile is shown of the lateral plane, imaged with a PMT. The three peaks are assumed to be originating from single photon hits. The maximum photon intensity can be estimated by dividing

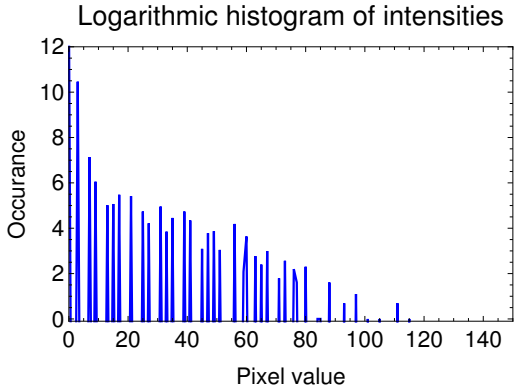

Figure 9 – Logarithmic histogram of the frame with the z-coordinate with the highest total intensity. The pixel value is proportional to the intensity. The image was taken with a 100× NA 1.35 glycerol objective with a matched Ps200 sample.

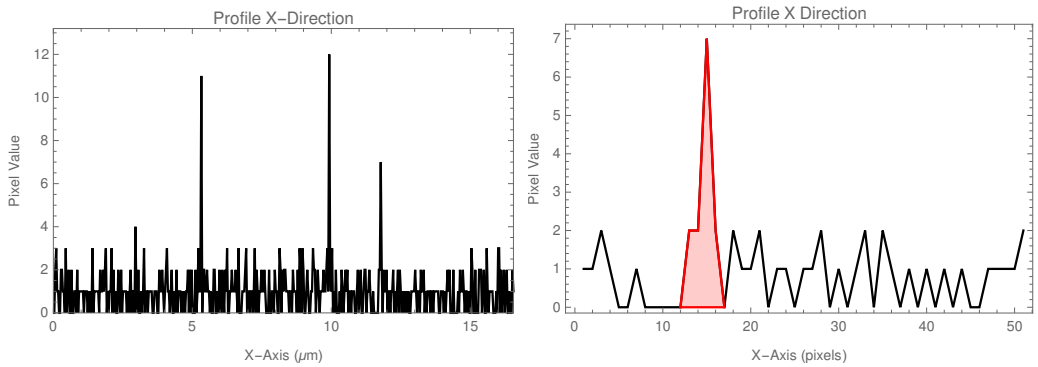

(a) Profile in the lateral plane. **(b)** Zoom of a single photon hit of Figure a.

Figure 10 – Profile of an image in the lateral plane some distance from a particle. The single hits are assumed to be single photon hits.

the maximum pixel value by the single photon hit. This yields a SNR between 4 and 7. For the deconvolution a SNR of 5 was used. For the Huygens deconvolution software the SNR is a parameter that can be changed in order to increase or decrease the level of detail at the cost of a higher noise. This means the SNR has little effect on the determined size of the PSF [25].

3.6 Deconvolution software

The deconvolution of the images to obtain the PSF was done by Huygens deconvolution software (version 15.10) created by SVI. To find the PSF the PSF distiller option was used. The distiller imports the voxel size, the numerical aperture, the backprojected pinhole, the wavelength of the excitation beam and of the emitted light from the Leica-X software (version 2.01 2015). The refractive indices of the immersion liquid and the embedding medium, the particle size and an estimate of the signal to noise ratio have to be entered manually. For the deconvolution a signal to noise ratio of 5 was used. In case of a refractive index mismatch between the objective and the sample, the position of the cover slip was entered as well.

To deconvolve an image with a PSF Huygens uses an algorithm silimlar to the van Cittert algorithm [26]. This involves making a guess of the deconvolved image using the Fourier transform of Equation 2.2. This image was convolved with the used PSF and compared to the image. The difference between the experimental data and the computationally convolved image can be used to improve the next guess of the image.

Open source deconvolution software PSFj (v2.0, build 236) was tested, but the SNR of the confocal images was too low to use this software, because PSFj focusses on brightfield images.

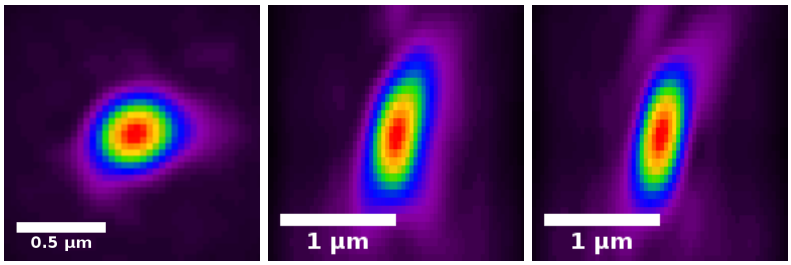

(a) XY-plane **(b)** XZ-plane **(c)** YZ-plane

Figure 11 – Point spread function of a 100× NA 1.40 oil objective on the Leica SP2 with imaged with PMT detectors.

3.7 Growth of the colloidal crystal

To check the calibration of the microscope, a colloidal crystal of RITC dyed silica particles was grown according to the method described by Jiang *et al.* [16]. To grow a crystal a sample of particles dispersed in ethanol was made. A cleaned Manzel Gläser # 1.5 cover slip cut in half along the long side was placed under a small angle into the colloidal suspension. The vial was placed under a glass beaker to prevent dust from contaminating the samples and to prevent moving air to disturb the constant evaporation speed. The evaporation of the ethanol takes a few days. During the evaporation the suspension was stored on a vibration free table. Crystals were grown for two particles, the Si450 and Si600 with two volume fractions 1% and 3%. According to Equation 2.9 this should yield for a 500 nm particle diameter for 1% and 3% volume percent 10 to 30 layers. To investigate how the evaporation time influences the crystal, another sample of Si450 particles with a volume fraction of 3% were dispersed in methanol.

To determine the interlayer distance of the crystal a FTIR spectrometer (Bruker Vertex 70) was used. The interlayer distance can be determined by the band gap in the transmission spectrum. For a crystal of spheres with a diameter of 468 nm, the band gap should be visible near a wavelength of $\lambda = 1020$ nm. To check whether a dip in transmission is due to the band gap or due to absorption the transmission spectrum of a monolayer was determined. The interlayer distance as measured by the confocal microscope was determined by calculating the average distance between the peaks of a z profile of am imaged volume. To check the diameter with the confocal microscope an intensity profile of a row of adjacent particles was used.

To image the crystal with the confocal microscope the particles were immersed in a glycerol/water mixture of 85% glycerol with a refractive index of $n_D^{20} = 1.451$ matched to the silica particles and placed onto a microscope slide. The crystal was imaged with a 100× NA 1.4 oil objective. The refractive index of the cover slip is matched to the immersion oil of the objective, so there is a mismatch in refractive index between the cover slip and the glycerol/water immersed particles.

4 Results and discussion

4.1 PSF of confocal microscope

In Figure 11 and Figure 12 the point spread functions for the Leica SP2 and Leica SP8 are shown. These are determined with an 100× oil objective with a numerical aperture of 1.4 and the same pinhole size of 1.00 AU and a matched sample. The size of the PSF for the SP8 microscope determined under the same conditions by Besseling [4] is 190 nm in the lateral direction and 490 nm in the axial direction. This is clearly lower than the obtained size of Table 2. Figure 13 is the PSF of a 100× NA 1.4 oil objective with a glycerol/water sample. The PSF of the SP2 looks tilted, because of a misalignment in the optics of the microscope. The PSF of the glycerol objective is skew, probably because this is an older, more worn objective. The skewness of the PSF's also affects the FWHM estimate of the size of the PSF, because for these two PSF's the size in the x-direction is not the same as the size in the y-direction, as can be seen in Table 2.

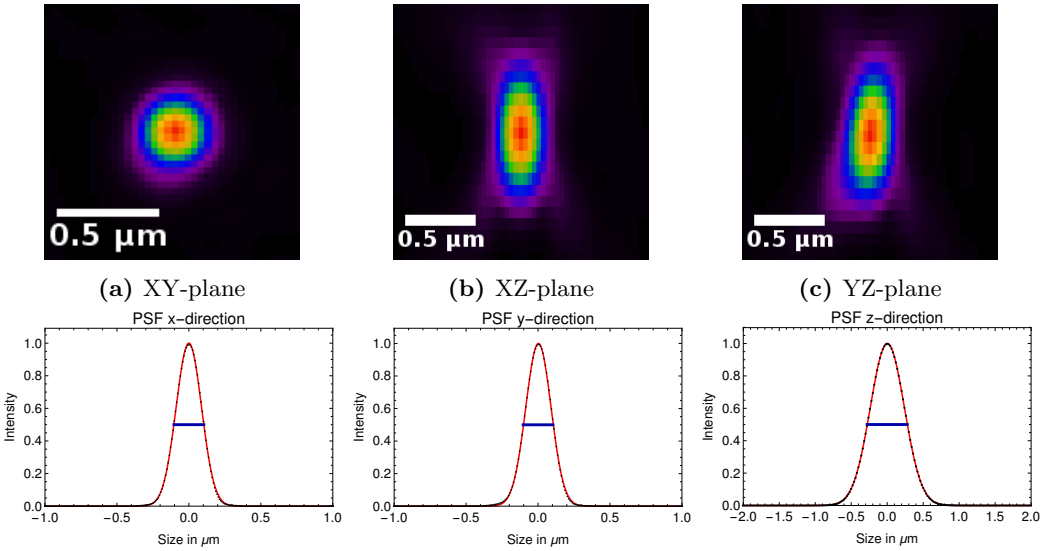

(a) XY-plane **(b)** XZ-plane **(c)** YZ-plane

(d) X-axis **(e)** Y-axis **(f)** Z-axis

Figure 12 – Point spread function of a 100× NA 1.40 oil objective on the Leica SP8 imaged with a HyD and a pinhole size of 1.0 AU. In Figure a, b and c the profiles with a FWHM is shown. This yiels a FWHM estimate of 210×210×560 nm^3.

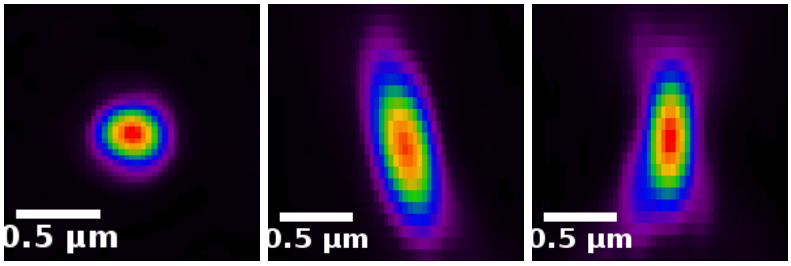

(a) XY-plane **(b)** XZ-plane **(c)** YZ-plane

Figure 13 – Point spread function of a 100× NA 1.35 glycerol objective and a matched glycerol/water sample on the Leica SP8 imaged with a HyD. A FWHM estimate yields a size of 300×190×520 nm.

Microscope	Objective	Embedding medium	FWHM PSF (nm)
SP2	100× NA 1.40 Oil	oil	290×260×600
SP8	100× NA 1.40 Oil	oil	210×210×560
SP8	100× NA 1.35 Glycerol	glycerol/water	300×190×520
SP8	100× NA 1.40 Oil	glycerol/water	280× 280×1 910
SP8	100× NA 1.35 Glycerol	oil	270× 270×1 710
Simulated	NA 1.4 Oil	glycerol/water	z: 1 516

Table 2 – Sizes of several PSF's using a FWHM estimate. The last size is the axial FWHM of the simulation of Sergey Loginov with a pinhole size of 1 AU.

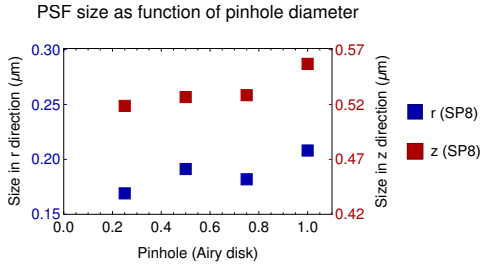

Figure 14 – FWHM estimate of PSF's determined with different pinhole sizes on the SP8 with a 100× NA 1.4 oil objective.

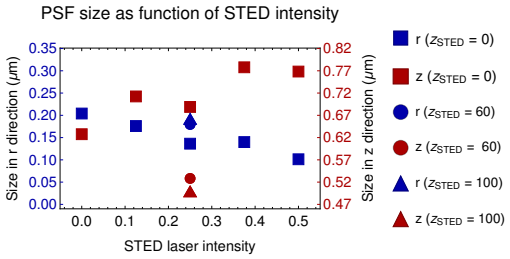

Figure 15 – FWHM estimates of the size of the PSF for different STED laser intensities and different z parameter values. The intensity is given as a fraction of the total laser capacity.

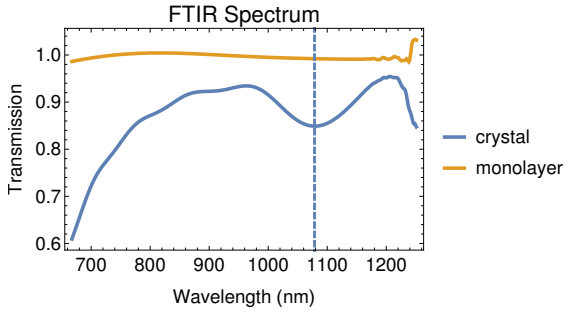

Figure 16 – Spectrum of the colloidal crystal with 5 to 6 layers created with Si450 particles with a diameter of 468 nm as determined with the TEM. The band gap is located at a wavelength of $\lambda = 1080$ nm.

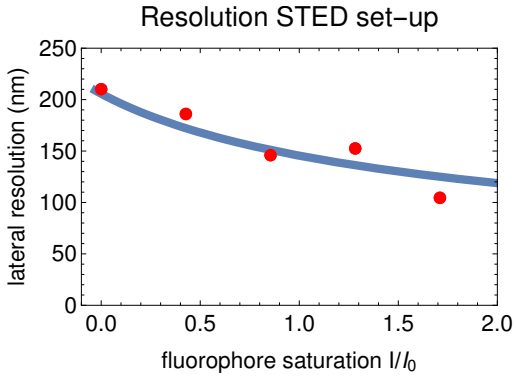

Figure 17 – Fit of Equation 2.8 with the axial resolutions of Figure 15 with a z parameter of 0, so the lateral resolution is optimized. The fluorophore saturation intensity I_s is according to this fit 30% of the maximum laser power.

4.2 Influence of the pinhole size

The dependence of the size of the PSF is shown in Figure 14. These are determined with a 100× NA 1.4 objective with the SP8 microscope. Although the size of the PSF decreases with smaller pinhole sizes, the effect is limited. This is unfortunate, because the smaller pinhole size greatly decreases the intensity of the detected light.

4.3 Mismatch in refractive index

The effect of the refractive index mismatch between the immersion liquid and the glass and embedding medium is not to be underestimated. The FWHM in the axial direction is very large, as listed in Table 2. These PSF's are shown in Figure 18 and 19. The interference patterns occur on the side of the objective if the embedding medium has a lower refractive index than the objective and vice versa. The higher order maxima are not visible in Figure 18 and 19, because Huygens does not support a deconvolution to a PSF of a custom height, therefore the z-profiles in Figure 20 are of a 200 nm particle, without deconvolution. Higher order maxima due to the interference are clearly visible. The experimental size of the PSF is larger than the simulated data, but the simulation also predicts a large size of the PSF in the axial direction.

4.4 PSF of STED microscopy

The sizes of the PSF using STED are shown in Figure 15. The size of the PSF depends on the z parameter. There does not seem to be much difference in the resolution between a z parameter of 60% or 100% in both the axial and the lateral direction. The resolution in the axial direction suffers for high STED laser intensities with a z parameter tuned to increase only the lateral resolution.

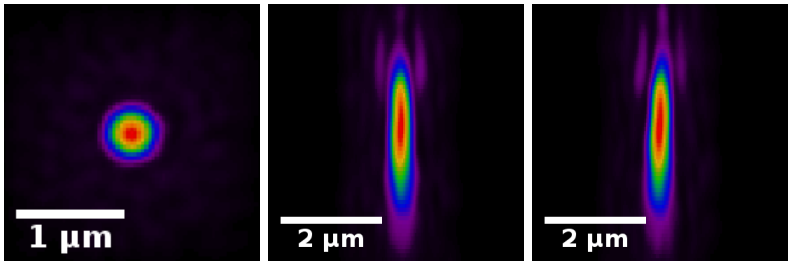

(a) XY-plane **(b)** XZ-plane **(c)** YZ-plane

Figure 18 – PSF of a 100× NA 1.35 glycerol objective and a matched oil sample. The objective is at the bottom.

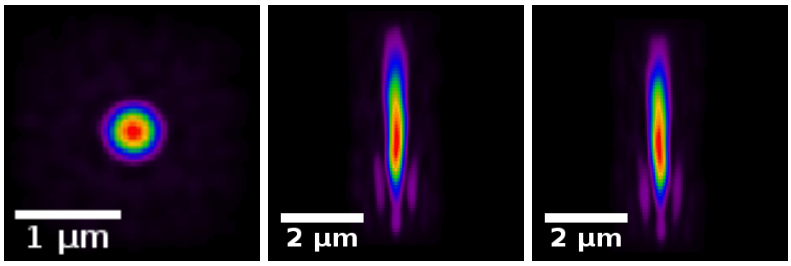

(a) XY-plane **(b)** XZ-plane **(c)** YZ-plane

Figure 19 – PSF of a 100× NA 1.4 oil objective and a matched glycerol/water sample. The objective is at the bottom.

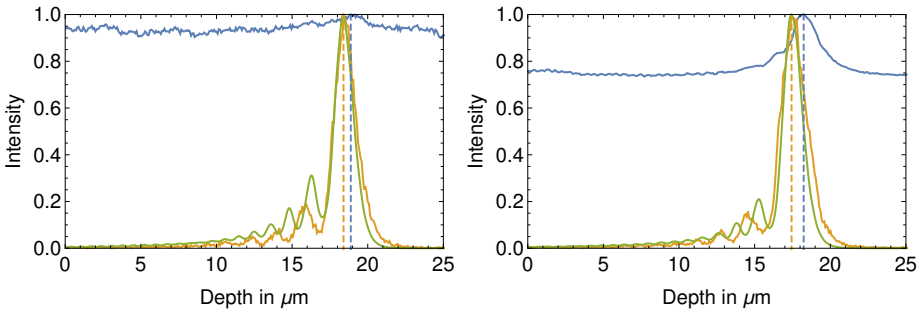

(a) Pinhole diameter 0.5 AU **(b)** Pinhole diameter 1.0 AU

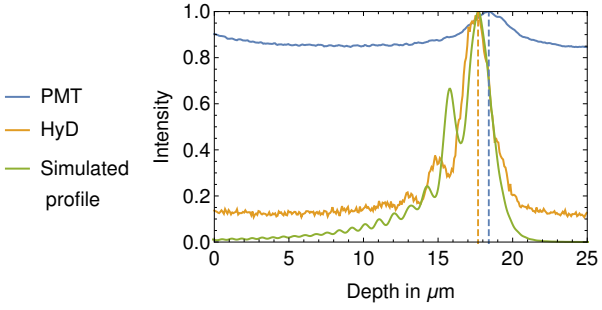

(c) Pinhole diameter 3.96 AU

Figure 20 – Averaged z profiles of an image of 200 nm FITC particles with a mismatch in refractive index between the cover slip and the immersion liquid. The refractive index of the glycerol/water embedding medium is $n_D = 1.451$ and the refractive index of the immersion oil is $n_D^{23} = 1.516$. The maximum of the PMT signal is the interface between the cover slip and the embedding medium. The green curve is a simulated PSF for the same parameters as used for the imaged z profiles using the method described in Appendix Appendix C. Simulated data courtesy of Sergey Loginov.

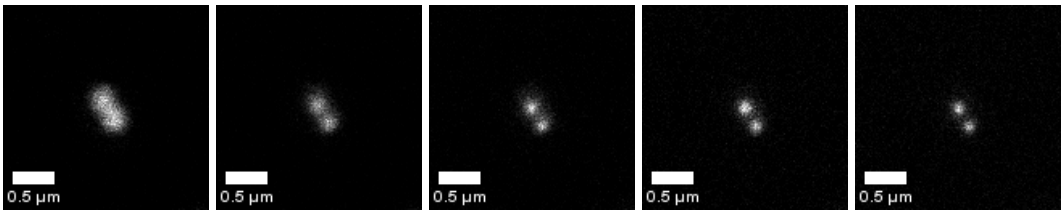

(a) 0% STED **(b)** 10% STED **(c)** 25% STED **(d)** 37.5% STED **(e)** 50% STED

Figure 21 – Improvement of resolution of an image of two particles next to each other. These images are made using a z factor of 0.

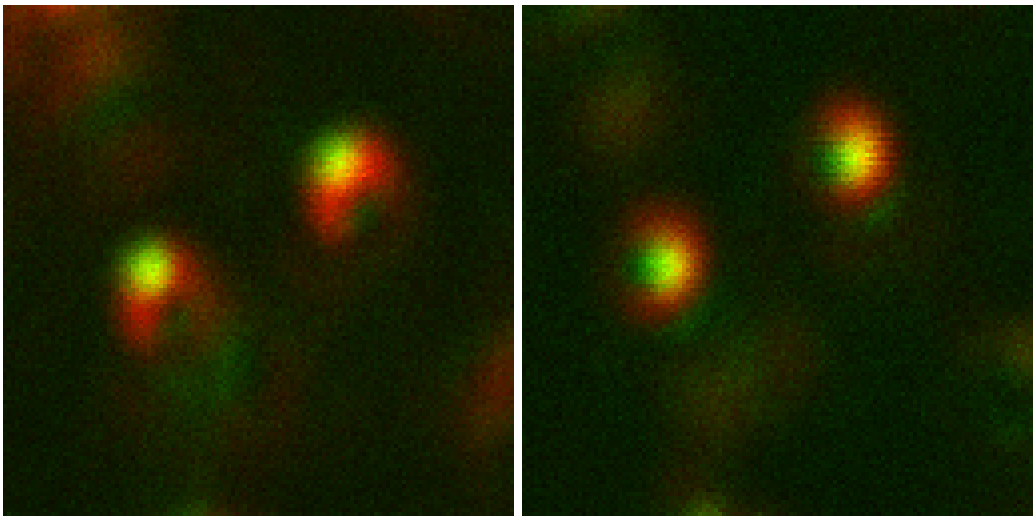

(a) Alignment before automatic aligning **(b)** Alignment after automatic aligning

Figure 22 – Reflectance of the excitation and depletion beam. The depletion beam is shown in red and the excitation beam in green.

Setting the z parameter to increase only the resolution in the axial direction does not seem to decrease the resolution in the lateral direction. To compare the dependence of the resolution on the laser intensity the resolutions are compared with Equation 2.8. The resolution could perhaps be higher with higher laser power, because the maximum resolution of 100 nm in the axial direction and 20 to 80 nm in the lateral direction [4] was not achieved. In Figure 17 the lateral resolutions are fitted. This gives an estimate that the saturation factor I_s is about 30% of the maximum laser power. The PSF with a z parameter of 60% looks like there is an mismatch in refractive index in the sample. This may be caused by an air bubble in the sample. An example of how the resolution improves is shown in Figure 21.

4.5 Alignment of the STED beam

The reflectance of the excitation and the depletion beam on a gold core is shown in Figure 22. Before the automatic alignment of the microscope the beams do not seem to align well enough to effectively use STED microscopy. After the automatic alignment the beams align better, but the beams do not perfectly overlap on the left side of the reflection shown in Figure 22b. The quality of the images can be improved by placing the particles into a spacer medium such as PVA. In this case the refection of the cover slip will not be visible. However, using PVA as medium there were non fluorescent dots present in the reflection channel. These reflections may be caused by water droplets which could not evaporate out of the PVA. An other possibility is that the PVA used for the sample was contaminated with gold nanoparticles. A misalignment in the STED beam could also explain the second maxima at the bottom of the PSF of the STED setup in Figure 27 in Appendix A, although a local mismatch in refractive index seems more likely.

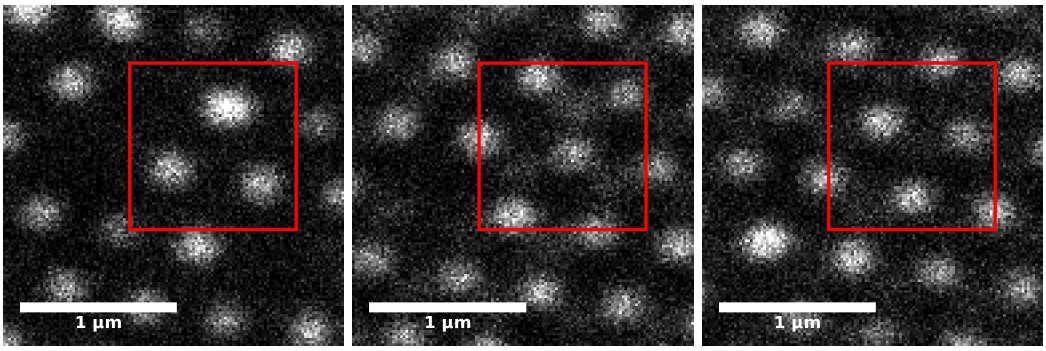

Figure 23 – Slices at different z-positions in the lattice at the same x and y positions. The first two images are taken 540 nm apart and the last two are separated by 420 nm. The position of the particles suggests a FCC lattice, because the triangle in the red box flipped between the first and the last image.

4.6 Colloidal crystal

The colloidal crystal forms either a FCC lattice or a HCP lattice as can be seen in Figure 23 and Figure 24. The Fourier transform of Figure 24d suggest hexagonal ordering. In Figure 16 the spectrum determined of a colloidal crystal of Si450 particles with an FTIR spectrometer is shown. It has a band gap at a wavelength of $\lambda = 1080$ nm. This corresponds to an interlayer distance of 404 nm and a particle diameter of 495 nm. Because the monolayer spectrum does not show a dip in transmission around $\lambda = 1080$ nm, the dip is due to Bragg diffraction. The gap however is broad, which could mean that there are not enough layers to determine the diffraction spectrum, that the interlayer distance varies or that the crystal is not perfectly perpendicular to the light beam. The axial profile of the crystal obtained with the confocal microscope yield an interlayer distance of 436 nm. This means the axial distance is elongated by a factor 1.08. The factor obtained by Equation 2.7 is 1.05. The geometrical formula of Visser *et al.* [10], Equation 2.6 gives a scale factor of 1.53. Using an effective numerical aperture of 0.7 of instead of 1.4 in Equation 2.6 as suggested by Besseling *et al.* [4] gives the same result as Equation 2.7. The difference is probably due to an inaccurate FTIR spectrogram. The small oscillations in the spectrum may be due to Fabry-Perot fringes [4]. If these are stronger they may be used for a more accurate measurement of the interlayer distance.

The particle diameter determined by averaging TEM images is 468 nm, which means that the diameter decreased with 5%. The increase in diameter compared to the diameter determined by averaging TEM images is probably due to a decrease in diameter due to evaporation of liquid inside the particle when doing TEM microscopy in vacuum. This means that the particle contains 18% volume percent solvent, in this case ethanol.

For the crystal grown with Si600 particles the colloids did form multiple layers, but were not crystalline enough. Although the cover slip was cleaned before crystallization, the particle size of 600 nm seems to high for growing a colloidal crystal using this method. Jiang *et al.* [16] did not grow particles with a diameter higher than 500 nm. The particle diameter with which a crystal can be formed can, however be increased by using other methods. Using sedimentation Hoogenboom *et al.*[27] used a particle diameter of 1.34 μm. To investigate the effect of the evaporation rate, a crystal was grown with methanol as solvent instead of ethanol. The particles dispersed in methanol did not form a crystal but formed layers of random ordering. The number of layers according to Figure 25 is 5 to 6 for a crystal grown with a suspension containing a particle volume percentage of 3%. According to Equation 2.9 the number of layers is 30. Equation 2.9 is determined for smaller particles than the 450 nm particles used, so the difference in layers may be due to the large particle diameter of the used partices. This difference could also mean that the cover slip or the vial were not entirely clean.

5 Conclusion

The size of the PSF decreases with a smaller pinhole, but for the quality of the image it may be that using a pinhole size lower than 1 AU does not improve the image much, because the area of

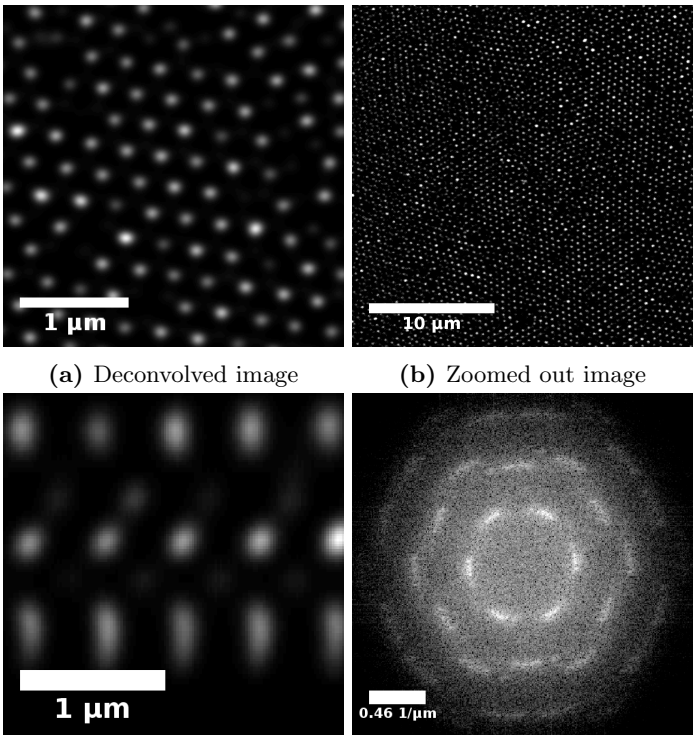

(a) Deconvolved image **(b)** Zoomed out image

(c) Slice of a row particles **(d)** Fourier transform of Figure b.

Figure 24 – Confocal images of the colloidal crystal of Si450 particles. Figure a and b are images in the lateral plane. Figure c is a slice taken of a line neighbouring particles in a deconvolved image. This slice suggest 5 layers and HCP ordering.

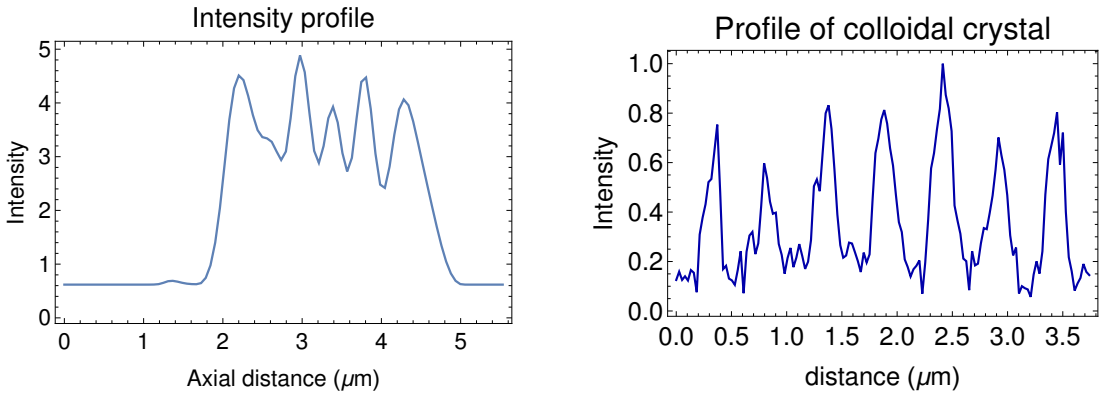

(a) Axial profile **(b)** Lateral profile

Figure 25 – Profiles of a crystal grown with Si450 particles. Figure a is a axial profile of the crystal. The average distance between the last 4 peaks is 436 nm. Figure b is a profile of neighbouring particles in the lateral plane. The average distance between the peaks is 481 nm.

the pinhole, and thus the intensity of the laser lowers with the square of the radius. A pinhole setting of 1 AU seems to be the most advantageous.

A mismatch in refractive index vastly increases the axial size of the PSF, when the mismatch occurs on the interface between the immersion liquid of the objective. The axial size is more than three times as large as the size of a PSF of a matched sample. The PSF is asymmetrical along the optical axis and consequently distorting images of a mismatched sample. The PSF has multiple observable maxima which is similar to theoretical predictions. The influence of the mismatch on the lateral shape and size seems limited.

STED microscopy increases the resolution, but using a STED configuration that only increases the lateral resolution spoils the resolution in the axial direction. Increasing the resolution in the axial direction does not seem to decrease the lateral resolution.

It it possible to create a colloidal crystal to calibrate the microscope. The axial distance seems a factor 1.08 larger due to elongation by the mismatch in refractive index. This is larger than the elongation factor found by Besseling of 1.05 [4]. A more accurate measurement is needed to determine if this is a significant difference, but it seems that the calibration of the microscope is 3% off. For the growth of the crystal it is important to use a clean surface on which the particles can adsorb and to use particles with a low polydispersity. Also it seems that a diameter of 600 nm is too large for a good crystallisation using the method of controlled drying.

6 Acknowledgements

First I would like my daily supervisor Ernest van der Wee. He was not reluctant to spend some time whenever I needed help with the microscope or the research in general. I also would like to thank Alfons van Blaaderen and Arnout Imhof for being my supervisors so I could do this research at the Soft Condensed Matter group. I would like to thank Marc Del Pozo Puig for the synthesis of the silica particles used to check the alignment of the STED beam and for the particles used for the colloidal crystal. I also thank him for his help with growing the crystal, the TEM images and the particle diameters of the used particles. I also would like to thank Jantina Fokkema for the synthesis of the particles used to determine the PSF of a STED image. Sergey Loginov also deserves my thanks for his simulated z profiles of a mismatched sample and his explanation of the effect of a mismatch on the PSF. I would like to thank Peter Helfferich for answering various questions about the microscope but particularly for his help with the FTIR spectrometer. He also made it possible for me to run the necessary computer software.

Appendix A Images of the PSF of a STED setup

These figures are the PSF's of a STED setup with different z parameter values. The shape of the PSF changes with a different z parameter to be more focussed in the lateral plane with a low z parameter and a small axial size with a high parameter.

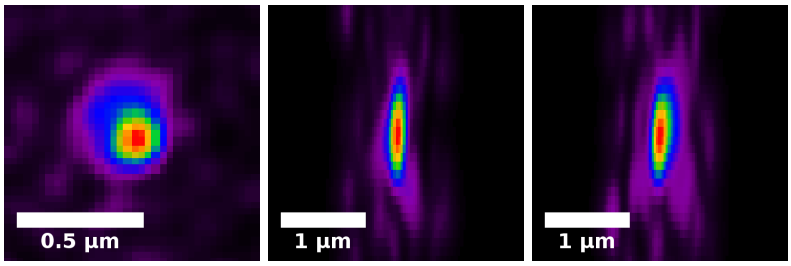

(a) XY-plane **(b)** XZ-plane **(c)** YZ-plane

Figure 26 – PSF of a 100× NA 1.4 oil objective with a z parameter set on 0% and 50% of the maximum STED laser intensity.

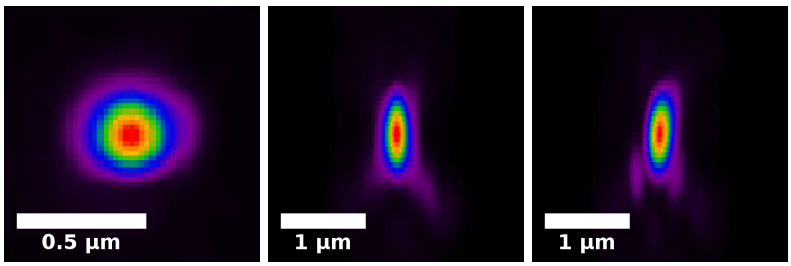

(a) XY-plane **(b)** XZ-plane **(c)** YZ-plane

Figure 27 – PSF of a 100× NA 1.4 oil objective with a z parameter set on 60% and 50% of the maximum STED laser intensity.

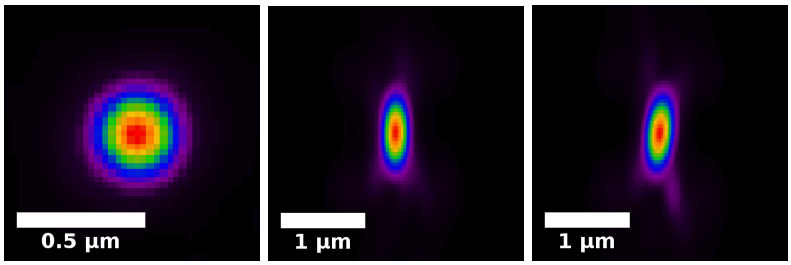

(a) XY-plane **(b)** XZ-plane **(c)** YZ-plane

Figure 28 – PSF of a 100× NA 1.4 oil objective with a z parameter set on 100% and 50% of the maximum STED laser intensity.

Appendix B Approximation of the point spread function

For the calculation of the PSF with a finite numerical aperture the approximation given by Robert H. Webb [2] was used.

$$\mathrm{PSF}_{confocal} = \left(|I_0|^2 + 2|I_1|^2 + |I_2|^2\right)^2$$

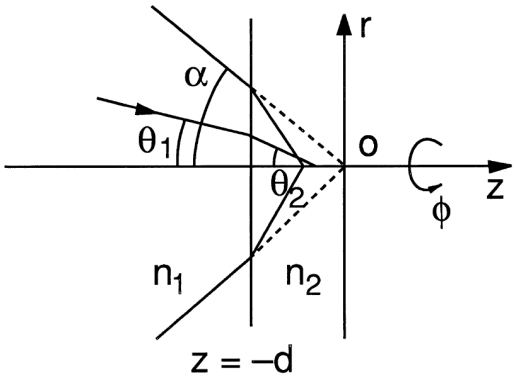

Figure 29 – Sketch by Sheppard *et al.* of the situation used for equation Equation Appendix C.1.

With I_0, I_1 and I_2 given by:

$$I_0(z,r) = \int_0^\theta J_0(rk' \sin\alpha)\sqrt{\cos\alpha}\, \sin\alpha(1+\cos\alpha)\, \exp(izk'\cos\alpha)\, \mathrm{d}\alpha$$
$$I_1(z,r) = \int_0^\theta J_1(rk' \sin\alpha)\sqrt{\cos\alpha}\, \sin^2\alpha\, \exp(izk'\cos\alpha)\, \mathrm{d}\alpha$$
$$I_1(z,r) = \int_0^\theta J_2(rk' \sin\alpha)\sqrt{\cos\alpha}\, \sin\alpha(1-\cos\alpha)\, \exp(izk'\cos\alpha)\, \mathrm{d}\alpha$$

Here $\sin\theta = \mathrm{NA}/n$ and $k' = 2\pi n/\lambda$. $J_{0,1,2}$ are Bessel functions. To evaluate the Bessel functions the following integral is calculated [28]:

$$J_n(x) = \int_0^\pi \cos(x\sin(\theta) - n\theta)\, \mathrm{d}\theta$$

Both the Bessel functions and the integrals $I_{0,1,2}$ are calculated by using the Simpson integration algorithm [29]:

$$\int_0^\theta f(x)\, \mathrm{d}x \approx \frac{\theta}{3N}\left(f(0) + f(\theta) + \sum_{n=1}^{2N-1}\left[4f(n\theta/(2N)) + 2f((n+1)\theta/(2N))\right]\right)$$

The functions $I_{0,1,2}$ have a dependence on r. To save computation time, the resulting PSF is interpolated when the pixel lies off the $y = 0$ or the $x = 0$ plane. This is possible, because the PSF is cylindrical symmetric around the z-axis. The grid size is 8 nm^3/voxel. The object is created by placing a 1 when the pixel is within the radius, this is in this case 200 nm, and 0 otherwise. The convolution is done by adding the calculated three dimensional PSF matrix for every pixel with a pixel value of 1 in the object to a newly created matrix.

Appendix C Point spread function of a mismatched sample

To calculate a PSF of a mismatched sample the equations of Appendix Appendix B can be modified to fit for a sample with a refractive index that does not fit the designed refractive index of the objective. Török*et al.* [30] use a vectorial approach to derive PSF for a mismatched sample. For the situation in Figure 29 [11] the equations become [11]:

$$\mathrm{PSF} = \left(I_0 + I_2\cos 2\phi\right)^2 + \left(I_2 \sin 2\phi\right)^2 + \left(-2iI_1\cos\phi\right)^2 \qquad \text{(Appendix C.1)}$$

For $\phi = \frac{1}{4}\pi$ this equation becomes simpler:

$$\mathrm{PSF} = |I_0|^2 + 2|I_1|^2 + |I_2|^2$$

With $I_{0,1,2}$ given by:

$$I_0 = \int_0^\alpha \sqrt{\cos\theta_1} \sin\,\theta_1 \exp\left[ik_0\Psi(\theta_1,\theta_2,-d)\right] \times (\tau_s + \tau_p\,\cos\theta_2) J_0\left(rk_1 \sin\theta_1\right) \exp\left(irk_2\,\cos\theta_1\right) \mathrm{d}\theta_1$$

$$I_1 = \int_0^\alpha \sqrt{\cos\theta_1} \sin\,\theta_1 \exp\left[ik_0\Psi(\theta_1,\theta_2,-d)\right] \times \tau_p \sin\theta_2\, J_1\left(rk_1 \sin\theta_1\right) \exp\left(irk_2 \cos\theta_2\right) \mathrm{d}\theta_1$$

$$I_2 = \int_0^\alpha \sqrt{\cos\theta_1} \sin\,\theta_1 \exp\left[ik_0\Psi(\theta_1,\theta_2,-d)\right] \times (\tau_s - \tau_p \cos\theta_2) J_2\left(rk_1 \sin\theta_1\right) \exp\left(irk_2\,\cos\theta_2\right) \mathrm{d}\theta_1$$

Here $k_0 = 2\pi/\lambda$ and $k_{1,2} = k_0 n_{1,2}$. n_1 is the refractive index of the objective and immersion fluid and n_2 the refractive index of the sample and d is the distance from the focus point without a mismatch to the focus point with the mismatch. $\theta_{1,2}$ are the half angle of the light cone in the immersion fluid of refractive index n_1 and the that of the sample of refractive index n_2. τ_p and τ_s are the Fresnel coefficients. Ψ is the aberration function given by:

$$\Psi(\theta_1,\theta_2,-d) = -d(n_1\cos\theta - n_2\cos\theta_2)$$

Because the excitation and emission wavelengths differ, the resulting PSF is the product of the excitation and the emission PSF. Both PSF's are convolved by the pinhole as it it projected on the focus point. This is 0 when inside the pinhole area and 1 within the area of pinhole [31].

$$\mathrm{PSF}_{confocal} = \mathrm{PSF}_{excitation} \times (\mathrm{PSF}_{emission} \circledast D_{pinhole})$$

Bibliography

[1] N. Martini, J. Bewersdorf, and S.W. Hell, A new high-aperture glycerol immersion objective lens and its application to 3d-fluorescence microscopy, *Journal of Microscopy*, 206(2):146–151, 2002.

[2] R.H. Webb, Confocal optical microscopy, *Reports on Progress in Physics*, 59:427–471, 1995.

[3] E. Abbé, Beitrage zur theorie des mikroskops und der mikroskopischen wahrnehmung, *Archiv fuer Mikroskopische Anatomie und Entwicklungsmechanik*, 9:413–420, 1883.

[4] T. Besseling, Self-assembly of colliodal spheres and rods in external fields, pages 20–41, 2014.

[5] S.W. Hell and J. Wichmann, Breaking the diffraction resolution limit by stimulated emission: stimulated-emission-depletion fluorescence microscopy, *Opt. Lett.*, 19(11):780–782, 1994.

[6] M. Ehrenberg, Super-resolved fluorescence microscopy, *Scientific Background on the Nobel Prize in Chemistry 2014*, 2014.

[7] D. Wildanger, R. Medda, L. Kastrup, and S.W. Hell, A compact sted microscope providing 3d nanoscale resolution, *Journal of Microscopy*, 236(1):35–43, 2009.

[8] Leica, Dual color sted imaging principles and tips & tricks, *Resolution, Confocal application letter*, (37), 2011.

[9] E.W. Weisstein, Convolution theorem, `http://mathworld.wolfram.com/ConvolutionTheorem.html`, 2016, accessed: 7-06-2016.

[10] T.D. Visser and J.L. Oud, Volume measurements in three-dimensional microscopy, *Scanning*, 16:198–200, 1994.

[11] C. J. R. Sheppard and P. Török, Effects of specimen refractive index on confocal imaging, *Journal of Microscopy*, 185:366–374, 1997.

[12] J.N. Farahani, M.J. Schibler, and L.A. Bentolila, Stimulated emission depletion (STED) microscopy: from theory to practice, *Microscopy: Science, Technology, Applications and Education*, pages 1539–1547, 2010.

[13] V. Westphal and S.W. Hell, Nanoscale resolution in the focal plane of an optical microscope, *Physical Review Letters*, 94(143903), 2005.

[14] Leica, Leica tcs sp8 sted 3x, *Product brochure*, 2014.

[15] S.W. Hell, Far-field optical nanoscopy, *Science*, 316:1153–1158, 2007.

[16] P. Jiang, J.F. Bertone, K.S. Hwang, and V.L. Colvin, Single-crystal colloidal multilayers of controlled thickness, *Chemistry of Materials*, 11:2132–2140, 1999.

[17] W. Heller, The determination of refractive indices of colloidal particles by means of a new mixture rule or from measurements of light scattering, *Physical Review*, 68(1-2):5–10, 1995.

[18] J. Thijssen, Characterization of photonic colloidal crystals in real and reciprocal space, pages 41–45, 2007.

[19] Wavelength-Tech, Ultraviolet grade fused silica, `http://www.wavelength-tech.com/IR-Optics/Material-JGS1.jsp`, 2012, accessed: 25-05-2016.

[20] N.G. Bastús, J. Comenge, and V. Puntes, Kinetically controlled seeded growth synthesis of citrate-stabilized gold nanoparticles of up to 200 nm: Size focusing versus ostwald ripening, *Langmuir*, 21:11098–11105, 2011.

[21] C. Graf, D.L.J. Vossen, A. Imhof, and A. van Blaaderen, A general method to coat colloidal particles with silica, *Langmuir*, 19:6693–6700, 2003.

[22] S. Link and M. A. El-Sayed, Size and temperature dependence of the plasmon absorption of colloidal gold nanoparticles, *The Journal of Physical Chemistry B*, 103:4212–4217, 1999.

[23] Leica, Leica hyd — photon counter — hybrid detector, `http://www.leica-microsystems.com/products/confocal-microscopes/details/product/leica-hyd/`, 2016, accessed: 6-06-2016.

[24] SVI, Nyquistcalculator — scientific volume imaging, `https://svi.nl/Nyquistcalculator`, 2016, accessed: 11-05-2016.

[25] SVI, Signal-to-noise ratio — scientific volume imaging, `https://svi.nl/SignalToNoiseRatio`, 2016, accessed: 25-05-2016.

[26] SVI, Non-linear iterative restoration methods — scientific volume imaging, `https://svi.nl/NonLinearIterativeMethod`, 2016, accessed: 6-06-2016.

[27] J.P. Hoogenboom, P. Vergeer, and A. van Blaaderen, A real-space analysis of colloidal crystallization in a gravitational field at a flat bottom wall, *Journal of Chemical Physics*, 119(6): 3371–3383, 2003.

[28] E.W. Weisstein, Bessel function of the first kind, `http://mathworld.wolfram.com/BesselFunctionoftheFirstKind.html`, 2016, accessed: 25-05-2016.

[29] E.W. Weisstein, Simpson's rule, `http://mathworld.wolfram.com/SimpsonsRule.html`, 2016, accessed: 17-05-2016.

[30] P. Török, P. Varga, and G.R. Booker, Electromagnetic diffraction of light focused through a planar interface between materials of mismatched refractive indices: structure of the electromagnetic field. i, *Journal of the Optical Society of America A*, 12(10):2136–2144, 1995.

[31] M. Gu and C.J.R. Sheppard, Effects of a finite-sized pinhole on 3d image formation in confocal two-photon fluorescence microscopy, *Journal of Modern Optics*, 40(10):2009–2024, 1993.